

Nanocavity optomechanical torque magnetometry and radiofrequency susceptometry

Marcelo Wu^{1,2†}, Nathanael L.-Y. Wu^{1,2†}, Tayyaba Firdous^{2,3†}, Fatemeh Fani Sani^{2,3}, Joseph E. Losby^{2,3}, Mark R. Freeman^{2,3*} and Paul E. Barclay^{1,2*}

Nanophotonic optomechanical devices allow the observation of nanoscale vibrations with a sensitivity that has dramatically advanced the metrology of nanomechanical structures^{1–9} and has the potential to impact studies of nanoscale physical systems in a similar manner^{10,11}. Here we demonstrate this potential with a nanophotonic optomechanical torque magnetometer and radiofrequency (RF) magnetic susceptometer. Exquisite readout sensitivity provided by a nanocavity integrated within a torsional nanomechanical resonator enables observations of the unique net magnetization and RF-driven responses of single mesoscopic magnetic structures in ambient conditions. The magnetic moment resolution is sufficient for the observation of Barkhausen steps in the magnetic hysteresis of a lithographically patterned permalloy island¹². In addition, significantly enhanced RF susceptibility is found over narrow field ranges and attributed to thermally assisted driven hopping of a magnetic vortex core between neighbouring pinning sites¹³. The on-chip magnetosusceptometer scheme offers a promising path to powerful integrated cavity optomechanical devices for the quantitative characterization of magnetic micro- and nanosystems in science and technology.

Torque magnetometry has seen a recent resurgence because of the miniaturization of mechanical devices¹⁴. The high detection sensitivity of resonant nanomechanical torque sensors has allowed for minimally invasive observations of magnetostatic interactions and hysteresis in a variety of magnetic materials, which include thin films¹⁵, mesoscale confined geometries that are deposited¹⁶ or epitaxially grown¹⁷, and small aggregates of nanoparticles¹⁸. Beyond the static limit, nanomechanical torque magnetometry has been extended to timescales that allow for the detection of slow thermally activated dynamics¹², a.c. susceptibility¹⁷ and magnetic resonance^{19,20}.

This powerful technique relies on the detection of the deflection of a mechanical element by angular momentum transfer that originates from magnetic torques $\tau = \mu_0 \mathbf{m} \times \mathbf{H}$, generated as the magnetic moments in the system \mathbf{m} experience an orthogonally directed component of the applied magnetic field \mathbf{H} . So far, improvements to torque magnetometers have been driven primarily by enhancements to the response of nanomechanical resonators that result from their low mass and high mechanical quality factor (Q_m). Readout of magnetically driven motion has involved detection through free-space optical interferometric methods with very low optical-quality factor ($Q_o \approx 1$) Fabry–Perot cavities formed between the nanomechanical resonator and its supporting substrate¹⁶. However, as device-dimensions scale down and the number of magnetic spins become too small or the dynamics too fast, the mechanical deflections become more difficult to detect. Migration to a more-sensitive readout scheme is essential. The integration of a nanoscale optical cavity offers a natural path for improvement.

Nanocavity–optomechanical devices enhance mechanical detection sensitivity by confining light to high- Q_o modes localized within the nanomechanical resonator. They have been exploited for metrology applications such as force and displacement detection^{2,3}, inertial sensing⁴, torque sensing^{5–7} and the observation of mechanical quantum fluctuations⁸. Recently, microscale ($\sim 10\text{--}100\,\mu\text{m}$) cavity optomechanical devices were combined with magnetostrictive materials to create external magnetic field sensors²¹. Nanophotonic optomechanical devices with subwavelength dimensions have tremendous potential to impact mechanical sensing of the microscopic electronic and magnetic dynamics of meso- and nanoscale systems typically using conventional readout optical methods^{10,11}. In this letter, we apply a nanocavity optomechanical sensor to a nanoscale condensed-matter system for the first time and demonstrate that torque magnetometry can be performed with sufficient sensitivity for the detection of Barkhausen features that were previously undetected in ambient conditions. We use this device to demonstrate a new form of nanomechanical RF susceptometry, and observe an enhanced magnetic susceptibility associated with single pinning and depinning events that can increase the torque magnetometer sensitivity by over an order of magnitude.

The high sensitivity of nanocavity optomechanical devices arises from a combination of large optomechanical coupling, large mechanical resonator susceptibility (low mass m_{eff} and large Q_m) and sharp optical-cavity response (large Q_o). The device employed here, an example of which is shown in Fig. 1a, is designed with these properties in mind. Referred to as a split-beam nanocavity (SBC)⁶, it consists of two suspended silicon photonic crystal nanobeams—one anchored in three sections, and the other ‘moving nanobeam’ anchored by two supports. This supports an optical mode whose field, shown in Fig. 1b, is confined to the central gap region and has a high Q_o ($\sim 5,000$ for the device studied here) owing to careful mode matching between the local field supported by the gap with the field in the elliptical holes of the nanobeams²². Vibrations of nanobeam mechanical resonances modulate both the gap width and the distance between the SBC and the fibre taper waveguide used to couple light evanescently into and out of the nanocavity, as illustrated in the experimental set-up in Fig. 2a (details in Methods). Of particular interest for torque magnetometry is the torsional resonance T_y of the moving nanobeam, where the nanobeam ends move anti-symmetrically out-of-plane, as shown schematically in Fig. 1a. This low mass ($m_{\text{eff}} = 1\,\text{pg}$) resonance (frequency $\omega_m/2\pi = 3\,\text{MHz}$) can be excited efficiently by nanoscale sources of torque coupled to the SBC.

The interaction between nanobeam motion and nanocavity optical dynamics is characterized by the optomechanical coupling coefficient g_{om} (see Supplementary Section 1). Detection of the vertical motion of the T_y resonance relies on the dispersive

¹Department of Physics and Astronomy and Institute for Quantum Science and Technology, University of Calgary, Calgary, Alberta T2N 1N4, Canada.

²National Institute for Nanotechnology, Edmonton, Alberta T6G 2M9, Canada. ³Department of Physics, University of Alberta, Edmonton, Alberta T6G 2E9, Canada. [†]These authors contributed equally to this work. *e-mail: freemanm@ualberta.ca; pbarclay@ucalgary.ca

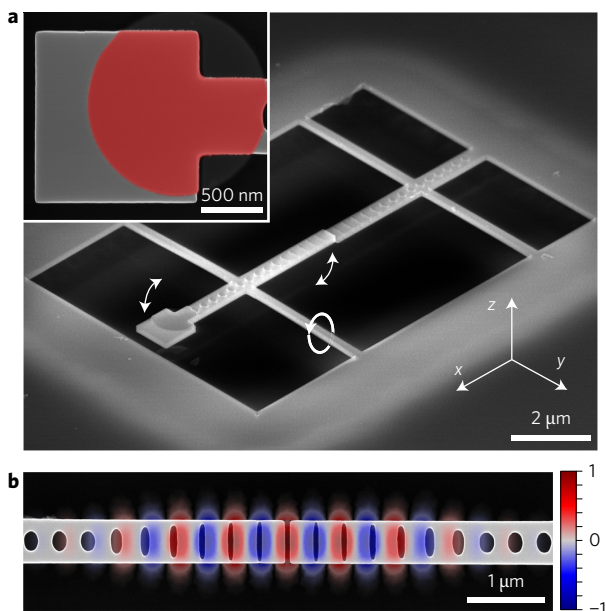


Figure 1 | Split-beam nanocavity. **a**, Tilted scanning electron micrograph (SEM) of a split-beam cavity optomechanical torque sensor supporting a 40 nm thick permalloy island (highlighted in red in the inset). **b**, Top-view SEM of the nanocavity overlaid with a finite-element simulation (COMSOL) of the normalized field distribution E_y of its optical mode.

optomechanical interaction between the SBC and the fibre taper. The fibre taper renormalizes the nominally symmetric nanocavity field and induces $g_{\text{om}}/2\pi$ in the gigahertz per nanometre range²³. The displacement sensitivity of the fibre-coupled SBC device can be calibrated by measuring the optomechanically transduced thermal motion, as shown in Fig. 2b,c. For typical operating conditions, it is in the tens of femtometres per $\text{Hz}^{1/2}$ range with an equivalent torque of $1.3 \times 10^{-20} \text{ N m} (\text{Hz}^{1/2})^{-1}$ (details in Supplementary

Sections 2 and 3). All the measurements are performed in ambient conditions, resulting in $Q_m < 100$ because of viscous air damping.

Nanocavity torque magnetometry can be performed by actuating the T_y mode with a magnetic field \mathbf{H} that interacts with a magnetic moment \mathbf{m} on the nanobeam, shown in the inset in Fig. 1a (Methods). When an in-plane static field $H_x^{\text{d.c.}}$ is applied, the permalloy becomes magnetized with a net moment $m_x(H_x^{\text{d.c.}})$ along the field x direction. By applying an additional RF field H_z^{RF} directed in the out-of-plane z direction, a magnetic torque τ_y is generated proportional to m_x and directed along the torsion rod that supports the moving nanobeam. When the RF field is applied at the T_y resonance angular frequency ω_m , the resulting driven beam displacement can be detected optomechanically from the nanocavity optical response. A typical signal is shown in the spectral domain in Fig. 2b, where it clearly emerges as a sharp peak at ω_m far above the thermomechanical noise. Although this device has the largest optomechanical magnetic transduction of those fabricated for this study, other devices (Supplementary Section 7) were observed to display behaviour similar to that described throughout this letter.

To perform magnetometry on the permalloy island, hysteresis loops were measured by varying $H_x^{\text{d.c.}}$ via translation of the permanent magnet while recording the optomechanically transduced RF signal for a fixed H_z^{RF} using the lock-in amplifier. Figure 3 shows the torque signal normalized to the value at saturation, with the corresponding scale for the net magnetization on the right axis. Beginning at high field (blue curve in Fig. 3), the magnetization was nearly saturated (section of the curve labelled A; the corresponding lettered frames in the bottom section of Fig. 3 are representations of the spin textures from micromagnetic simulation (Methods)). As the field decreases, three large discontinuities in the net moment inferred from the optomechanical signal are observed and correspond to irreversible changes in the spin texture, beginning with nucleation of a magnetic vortex with an out-of-plane core surrounded by in-plane curling magnetization (section B of the curve in Fig. 3). As

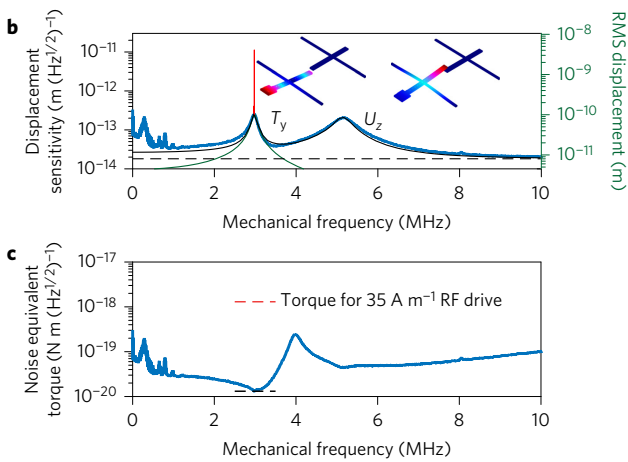
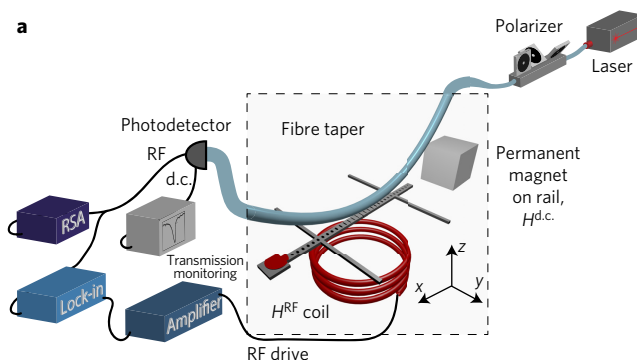


Figure 2 | Measurement set-up and spectral response. **a**, Experimental set-up for nanocavity optomechanical torque magnetometry measurements (not to scale). All the measurements are performed in an ambient nitrogen-purged environment (grey region). A dimpled fibre taper is used to probe the optomechanical nanocavity. A permanent magnet with an adjustable position provides varying static magnetic fields. The lock-in amplifier reference is power amplified and sent to coils below the device to create an RF magnetic field in the z direction. **b**, Displacement density (left axis) from the real-time spectrum analyser (RSA) that shows thermally driven mechanical modes T_y and U_z (blue) and the magnetically driven signal (narrow peak highlighted in red) generated by a magnetic driving field H_z^{RF} of 35 A m^{-1} applied with the permalloy island magnetization saturated by $H_x^{\text{d.c.}}$. Black lines are fits to the T_y and U_z Lorentzian-shaped peaks (solid line) and the measurement noise floor (dashed line). The green curve (right axis) indicates the predicted root mean squared displacement of the T_y resonance in the presence of a 35 A m^{-1} RF magnetic field as a function of frequency. Insets show simulated displacement profiles of T_y and U_z . **c**, Torque equivalent noise of the thermomechanical displacement signal in **b**. The red dotted line indicates the predicted torque in the presence of a 35 A m^{-1} H_z^{RF} field, and is labelled by the values on the left axis, assuming a 1 s integration time.

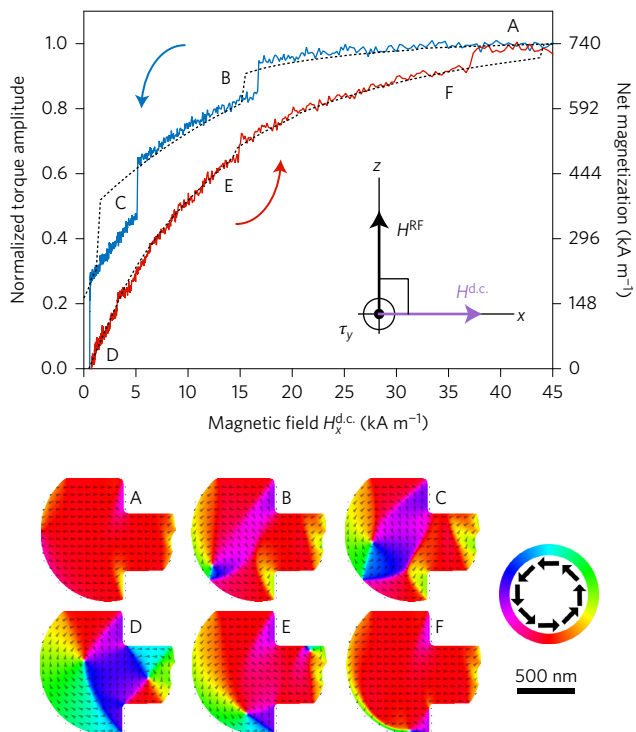


Figure 3 | Magnetic hysteresis of the permalloy island. Magnetization response of the permalloy element with a varying applied d.c. field along x (five-run average). The RF drive field is $H_z^{\text{RF}} = 35 \text{ A m}^{-1}$. The solid blue trace is a decreasing field sweep and the solid red trace is an increasing field sweep. Results from micromagnetic simulations of the permalloy island (highlighted in red in the SEM inset in Fig. 1a and also used as the simulation mask) are plotted with black dashed lines. The bottom panel shows simulated magnetization textures at different points in the hysteresis loop. The colour wheel shows the in-plane direction of magnetization, with red parallel to the applied d.c. field.

the d.c. field is further decreased, the vortex core translates towards the centre of the element until an intermediate texture arises; it features pronounced closure domains along the short edges perpendicular to the applied field (section C). The transition near zero field forms a two-vortex state, shown in frame D of Fig. 3, where the permalloy island's mushroom-like shape supports a Landau state in the stem (right side) and a distorted circular vortex in the cap (left side)²⁶, in keeping with the demagnetizing energetic preference for the moments near edges to be nearly tangential to the boundaries. When $H_x^{\text{d.c.}}$ is subsequently increased (red curve in Fig. 3), the net moment increases monotonically with the applied field. In section D of the simulation the two vortex cores move in opposite directions perpendicular to the field because the two circulations have opposite chiralities in this instance. The simulation frames E and F (Fig. 3) show the spin configurations just before each individual vortex core annihilates after the field-increasing sweep has pushed them too close to the edge to remain stable. The simulated hysteresis loop (black dashed line in Fig. 3) shows good qualitative agreement with observation, with the difference in the transition-field values in part because the simulations were performed without including thermal energy.

Figure 4 demonstrates the ability of the nanocavity optomechanical torque sensor to capture, in high-resolution measurements, the fine structure in the hysteresis that is the fingerprint of intrinsic disorder unique to a given permalloy island, and cannot be predicted by the idealized micromagnetic simulations described above. The high energy density of vortex cores makes them susceptible to pinning at imperfections (surface roughness and grain

boundaries) in the polycrystalline island. With diameters on the order of tens of nanometres, the cores finely probe the magnetic landscape as their positions change with applied field¹². Pinning and depinning events are captured as Barkhausen steps, with notable reductions in slope of the hysteresis curve seen when the cores are pinned. Figure 4 shows a rich spectrum of repeatable events whose character varies depending on the orientation of H_z^{RF} , as indicated in each of Fig. 4a–e. Repeatable events for H_z^{RF} perpendicular to the permalloy film (that is, along z) visible in section D of Fig. 3 are shown in close-up in Fig. 4d. If the applied field is kept below the first vortex-core annihilation field, curves like Fig. 4d show distinct steps without hysteresis when the field strength is ramped down. The absence of any minor hysteresis at each step is the result of very rapid (in comparison with the measurement bandwidth) thermally activated hopping between neighbouring pinning centres^{12,13}, such that the apparatus records a temporal average weighted by the relative dwell times in the two sites.

For non-normal H_z^{RF} , the nanocavity torque sensor can function as a susceptometer that probes RF magnetic susceptibility and provides new insight into the properties of the pinning processes. For these measurements, an in-plane x component of the RF field (parallel to the nominal d.c. field direction) is introduced by tuning the relative RF coil position off-centre to the device (details are given in Supplementary Section 5). Adjusting the relative chip-coil position is simplified experimentally by the ambient operating conditions and fibre-based readout. A small out-of-plane d.c. field $H_z^{\text{d.c.}}$ combines with the oscillating field H_x^{RF} to generate torque in the y direction proportional to the in-plane susceptibility. Signals recorded using both z and x components of the RF drive contain both torque contributions—from the net moment along x ($\propto m_x^{\text{d.c.}} H_z^{\text{RF}}$) and from the RF susceptibility along x ($\propto \chi_x^{\text{RF}} H_x^{\text{RF}} H_z^{\text{d.c.}}$), where χ is the magnetic susceptibility tensor of the permalloy island (see Supplementary Section 5).

Figure 4a,b shows the full hysteresis loops for two different RF field orientations, 45° (Fig. 4a) and 170° (Fig. 4b) anticlockwise from the horizontal. The torque values remain normalized to the 90° orientation. Corresponding close-ups of the low-field sections are shown in Fig. 4c,e. The peaks and dips newly found in the data are RF-susceptibility signatures that arise when the energy barrier between neighbouring pinning sites is small enough that the in-plane RF field is able to drive the core synchronously back-and-forth. To the best of our knowledge, these measurements are the first report of RF susceptibility due to the Barkhausen effect at the single pinning event level, though averaged events have been studied previously²⁷. The larger transitions between spin textures in the main loop are irreversible and therefore exhibit no accompanying RF susceptibility features. The effective susceptibility (calculated in Supplementary Section 6) $\partial m / \partial H$ will be largest when the RF drive amplitude is just above the threshold required for a synchronous response, where the ratio of ∂m (set to first approximation by the moment change at the Barkhausen jump) to ∂H is largest. Observed enhancements of up to 25 times over the susceptibilities when the core is pinned suggest RF-susceptibility engineering in applications such as field-sensing magnetometry and detecting small volumes of magnetic material.

Both the ratios of amplitudes and the relative signs of the net moment and susceptibility contributions in Fig. 4 are consistent with the changes of the RF field direction. Implementation of a scheme with an independent control of RF field components will enable quantitative separation of the susceptibility and magnetometry components through π phase shifts of individual RF drives without changing anything else, which provides further confirmation of the phenomena reported above. A proof-of-principle demonstration of our ability to probe different components of the susceptibility through reconfiguration of the RF field direction is presented in Supplementary Section 7, where the off-diagonal susceptibility of

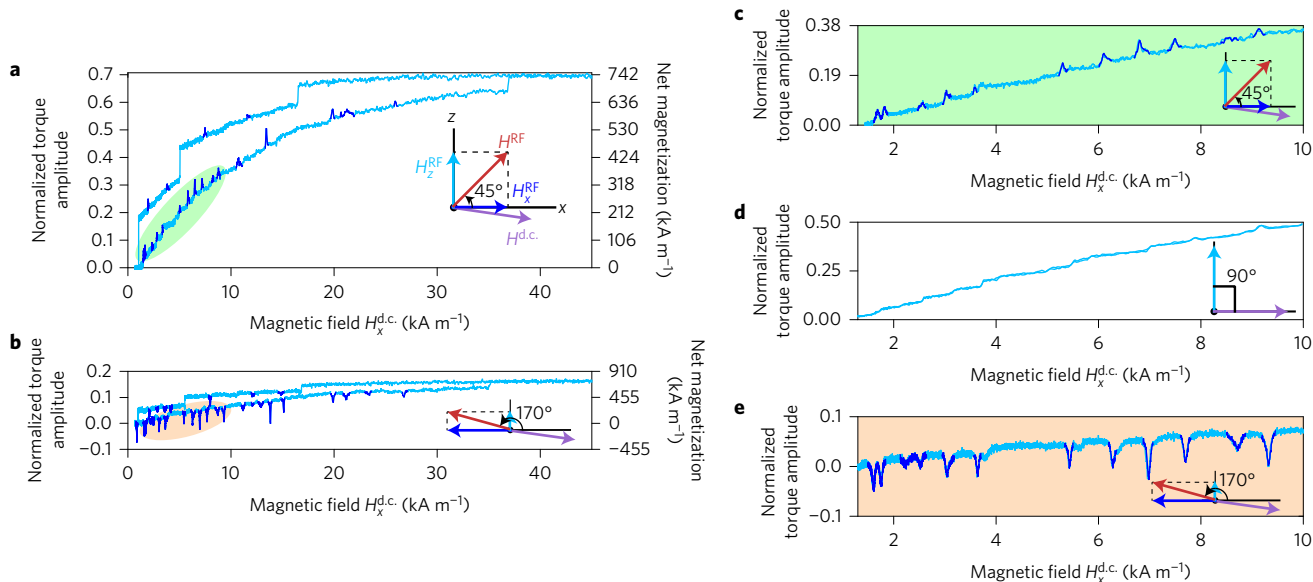


Figure 4 | Enhanced room-temperature magnetic susceptibility at Barkhausen steps. **a,b**, Hysteresis sweep with H^{RF} set to 45° (equal and same sign x and z components) (**a**) and 170° (opposite signed x and z components) (**b**). A select number of upward and downward peaks are highlighted in blue to show the contribution to the torque from susceptibility. **c–e**, Low-field $H_x^{d.c.}$ single forward and backward sweeps at three H^{RF} positions, 45° (**c**), 90° (**d**) and 170° (**e**). In all cases, the drive field $H^{RF} = 35 \text{ A m}^{-1}$.

the pinning events is detected in this way. Given the already important role of thermally driven rapid hopping in eliminating the observed minor hysteresis at Barkhausen steps¹², the synchronization must be thermally assisted. Operating the device at a low temperature in future work is required to search for the threshold behaviour.

The ability of the optomechanical nanocavity to detect nanoscale magnetic phenomena arises from its torque sensitivity of $1.3 \times 10^{-20} \text{ N m} (\text{Hz}^{1/2})^{-1}$, which at field strengths on the order of the Earth's field (44–60 µT), corresponds to a magnetic moment sensitivity of $(2.4 \pm 0.4) \times 10^7 \mu_B$. A minimum detectable volume of magnetic material of $0.015 \pm 0.005 \mu\text{m}^3$ is calculated for the largest susceptibility enhancement; increasing the RF drive would allow for the measurement of even smaller volume samples. Despite operating in ambient conditions, this device is of comparable or better sensitivity than previous nanoscale torque magnetometry devices^{12,16,20} reliant on free-space reflectometry and vacuum or cryogenic operation. Furthermore, its relatively low Q_m and megahertz operating frequency, in principle, allows megahertz bandwidth excitation and detection. Among nanoscale optomechanical torque metrology devices, the demonstrated sensitivity is only surpassed by systems that operate in vacuum⁷ or cryogenic conditions²⁸, none of which have yet been used for magnetometry or to probe nanoscale condensed-matter systems.

Notwithstanding the practical advantages enabled by operation in ambient conditions, vacuum and low temperature T_b will reduce the thermal force fluctuations that scale with $\sqrt{T_b/Q_m}$ and limit the sensitivity⁶. For example, $Q_m = 10^3$ – 10^4 for similar SBC devices has been observed in vacuum⁶, and $Q_m = 10^5$ has been observed at liquid helium temperatures for silicon zipper nanocavity devices²⁹. This indicates that a 10^4 improvement in the thermally limited sensitivity may be within reach. Even a modest improvement in sensitivity by an order of magnitude, in combination with a maximum driving field of 1 kA m^{-1} , could produce magnetic moment sensitivities below $2 \times 10^5 \mu_B$ (ref. 5), which enables nanomagnetism lab-on-a-chip studies of a wide range of systems^{10,11}.

In conclusion, we have demonstrated experimentally nanocavity optomechanical detection for torque magnetometry and RF susceptibility. The device presented here enabled a detailed study, under

ambient conditions, of the magnetostatic response and thermally assisted driven vortex-core hopping dynamics in a mesoscopic permalloy element under an applied field. This torque magnetometry technique complements other device-based nanoscale magnetic probes. Compared with planar micro-Hall approaches³⁰, which have been used to probe single pinning sites but have not been used to measure RF susceptibility, nanocavity torque magnetometry offers a higher frequency operation. Although it has yet to offer the single-spin sensitivity of nitrogen-vacancy-centre based imaging^{31,32}, it provides a comparatively fast acquisition of net magnetization, which allows measurement of magnetic hysteresis and susceptibility. Reconfiguration of the RF fields allows the probing of enhanced susceptibility components of single pinning events, and demonstrates that this magnetometry approach fulfils key requirements for an optomechanical lab-on-a-chip for nanomagnetism.

Methods

Methods and any associated references are available in the online version of the paper.

Received 6 May 2016; accepted 19 September 2016; published online 31 October 2016

References

- Li, M. *et al.* Harnessing optical forces in integrated photonic circuits. *Nature* **456**, 480–484 (2008).
- Liu, Y., Miao, H., Aksyuk, V. & Srinivasan, K. Wide cantilever stiffness range cavity optomechanical sensors for atomic force microscopy. *Opt. Express* **20**, 18268–18280 (2012).
- Anetsberger, G. *et al.* Measuring nanomechanical motion with an imprecision below standard quantum limit. *Phys. Rev. A* **82**, 061804 (2010).
- Krause, A. G., Winger, M., Blasius, T. D., Lin, W. & Painter, O. A high-resolution microchip optomechanical accelerometer. *Nat. Photon.* **6**, 768–772 (2012).
- Kim, P. H. *et al.* Nanoscale torsional optomechanics. *Appl. Phys. Lett.* **102**, 053102 (2013).
- Wu, M. *et al.* Dissipative and dispersive optomechanics in a nanocavity torque sensor. *Phys. Rev. X* **4**, 021052 (2014).
- Li, H. & Li, M. Optomechanical photon shuttling between photonic cavities. *Nat. Nano.* **9**, 913–919 (2014).
- Chan, J. *et al.* Laser cooling of a nanomechanical oscillator into its quantum ground state. *Nature* **478**, 89–92 (2011).
- Zhang, X., Zou, C. L., Jiang, L. & Tang, H. X. Cavity magnomechanics. *Sci. Adv.* **2**, 1501286 (2016).

10. Rugar, D., Budakian, R., Mamin, H. & Chui, B. Single spin detection by magnetic resonance force microscopy. *Nature* **430**, 329–332 (2004).
11. Bleszynski-Jayich, A. C. *et al.* Persistent currents in normal metal rings. *Science* **326**, 272–275 (2009).
12. Burgess, J. A. J. *et al.* Quantitative magnetomechanical detection and control of the Barkhausen effect. *Science* **339**, 1051–1054 (2013).
13. Compton, R. L. & Crowell, P. A. Dynamics of a pinned magnetic vortex. *Phys. Rev. Lett.* **97**, 137202 (2006).
14. Moreland, J. Micromechanical instruments for ferromagnetic measurements. *J. Phys. D* **36**, R39–R51 (2003).
15. Lim, S.-H. *et al.* Magneto-mechanical investigation of spin dynamics in magnetic multilayers. *Europhys. Lett.* **105**, 37009 (2014).
16. Davis, J. P. *et al.* Nanotorsional resonator torque magnetometry. *Appl. Phys. Lett.* **96**, 072513 (2010).
17. Losby, J. E. *et al.* Nanomechanical AC susceptometry of an individual mesoscopic ferrimagnet. *Solid State Comm.* **198**, 3–6 (2014).
18. Firdous, T. *et al.* Nanomechanical torque magnetometry of an individual aggregate of 350 nanoparticles. *Can. J. Phys.* **93**, 1–5 (2015).
19. Ascoli, C. *et al.* Micromechanical detection of magnetic resonance by angular momentum absorption. *Appl. Phys. Lett.* **69**, 3920–3922 (1996).
20. Losby, J. E. *et al.* Torque-mixing magnetic resonance spectroscopy. *Science* **350**, 798–801 (2015).
21. Forstner, S. *et al.* Ultrasensitive optomechanical magnetometry. *Adv. Mater.* **26**, 6348–6353 (2014).
22. Hryciw, A. C. & Barclay, P. E. Optical design of split-beam photonic crystal nanocavities. *Opt. Lett.* **38**, 1612–1614 (2013).
23. Hryciw, A. C., Wu, M., Khanaliloo, B. & Barclay, P. E. Tuning of nanocavity optomechanical coupling using a near-field fiber probe. *Optica* **2**, 491–496 (2015).
24. Rigue, J., Chrischon, D., de Andrade, A. M. H. & Carara, M. A torque magnetometer for thin films applications. *J. Magn. Magn. Mater.* **324**, 1561–1564 (2012).
25. Losby, J. E. *et al.* Nanomechanical torque magnetometry of permalloy cantilevers. *J. Appl. Phys.* **108**, 123910 (2010).
26. Cowburn, R. P., Koltsov, D. K., Adeyeye, A. O., Welland, M. E. & Tricker, D. M. Single-domain circular nanomagnets. *Phys. Rev. Lett.* **82**, 1042–1045 (1999).
27. Abu-Libdeh, N. & Venus, D. Dynamics of domain growth driven by dipolar interactions in a perpendicularly magnetized ultrathin film. *Phys. Rev. B* **81**, 195416 (2010).
28. Kim, P. H., Hauer, B. D., Doolin, C., Souris, F. & Davis, J. P. Approaching the standard quantum limit of mechanical torque sensing. Preprint at <https://arxiv.org/abs/1607.00069> (2016).
29. Safavi-Naeini, A. *et al.* Squeezed light from a silicon micromechanical resonator. *Nature* **500**, 185–189 (2013).
30. Rahm, M., Biberger, J., Umasky, V. & Weiss, D. Vortex pinning at individual defects in magnetic nanodisks. *J. Appl. Phys.* **93**, 7429–7431 (2003).
31. Teteigne, J.-P. *et al.* Nanoscale imaging and control of domain-wall hopping with a nitrogen-vacancy center microscope. *Science* **344**, 1366–1369 (2014).
32. Rugar, D. *et al.* Proton magnetic resonance imaging using a nitrogen-vacancy spin sensor. *Nat. Nano.* **10**, 120–124 (2015).

Acknowledgements

This work is supported by the Natural Science and Engineering Research Council of Canada, Canada Research Chairs, the Canada Foundation for Innovation and Alberta Innovates Technology Futures. Many thanks to A. Hryciw, M. Mitchell, M. Belov and D. Fortin for their technical contributions. We also thank the staff of the nanofabrication facilities at the University of Alberta and at the National Institute for Nanotechnology as well as the machinists at the University of Calgary Science Workshop for their technical support.

Author contributions

P.E.B. and M.R.F. conceived and supervised the project. M.W. and N.L.-Y.W. designed and fabricated the devices. N.L.-Y.W. imaged the devices. M.W. set up the measurement equipment, including the fibre taper. M.W., N.L.-Y.W. and T.F. performed measurements on the device. M.W., N.L.-Y.W., T.F. and F.F. analysed the data. M.W. and N.L.-Y.W. prepared the figures. F.F. and T.F. contributed simulations to the manuscript. F.F. helped with the theoretical framework for the RF susceptibility mixing scheme in the supplementary material. J.E.L. provided guidance and technical assistance with the instrumentation and measurements. All the co-authors contributed to and proofread the manuscript.

Additional information

Supplementary information is available in the online version of the paper. Reprints and permissions information is available online at www.nature.com/reprints. Correspondence and requests for materials should be addressed to M.R.F. and P.E.B.

Competing financial interests

The authors declare no competing financial interests.

Methods

Permalloy deposition. Permalloy structures with a thickness of 40 nm were patterned onto undercut SBC devices using ultrahigh vacuum collimated deposition and a lift-off process³³. The pad of area $1.4 \times 1.3 \mu\text{m}$ is partially covered with permalloy because of the imperfect lithographic alignment during the lift-off process, which results in the ‘mushroom’ shape of the island. As the polycrystalline permalloy is optically absorbing, the permalloy island is positioned far from the nanocavity centre, where it does not degrade Q_0 by interacting directly with the nanocavity optical mode.

Measurement set-up. To perform nanocavity-optomechanical torque magnetometry, a permanent magnet (N50 neodymium iron boron, 2.5 cm^3) was mounted on a motorized stepper rail and used to apply a stable and finely adjustable $H_x^{\text{d.c.}}$. The field magnitudes were recorded with a three-axis Hall probe placed below the sample chip (Sentron 3M12-2). The RF coil positioned beneath the sample chip was used to generate H_z^{RF} and H_x^{RF} . This coil was integrated into an optical fibre-taper probing set-up identical to that used in previous nanophotonic cavity optomechanics experiments⁶. The schematic of the set-up presented in Fig. 2a illustrates the detection of the nanobeam motion through a dimpled optical fibre taper (more details given in Supplementary Section 1). The dimple is positioned in contact with the top surface of the fixed nanobeam such that, in the vicinity of the nanocavity gap region, the fibre taper is aligned $<200 \text{ nm}$ from the device, where it induces significant dispersive optomechanical coupling²³ and evanescently couples light into and out of the nanocavity. The optical transmission of a tunable laser source (Santec TSL-510, wavelength range 1,500–1,630 nm) through the fibre taper was detected using a low-noise photodetector (New Focus 1811) and analysed using

a real-time spectrum analyser (Tektronix RSA 5103B) and lock-in amplifier (Zurich Instruments HF2LI). For driving the RF coil, a reference tone was passed from the lock-in amplifier through an RF power amplifier (ENI 403 L, 37 dB gain). All the measurements were conducted at ambient temperature and pressure within a nitrogen-purged environment.

Micromagnetic simulations. Landau–Lifshitz–Gilbert-based micromagnetic simulations were performed with MuMax 3.5 GPU-accelerated open-source software³⁴ using a three-dimensional grid size of 5 nm and the characteristic thin-film properties of permalloy—saturation magnetization $M_s = 780 \text{ kA m}^{-1}$ and an exchange stiffness constant $A_{\text{ex}} = 13 \text{ pJ m}^{-1}$. From the calibration of a similar permalloy film (under the same conditions), an experimental value of $M_s = 770 \text{ kA m}^{-1}$ was obtained. However, as the calibrated film was not deposited at the same time as the permalloy pad under study here, there is some uncertainty in the value of M_s . The Gilbert damping constant was set to $\alpha = 1$ to minimize the simulation time required for the quasistatic hysteresis. From the simulations, the net magnetization of the structure at an applied field of 45 kA m^{-1} was found to be $M = 0.965M_s$, and this number was assumed also to be representative for the experiment.

References

33. Diao, Z. *et al.* Stiction-free fabrication of lithographic nanostructures on resist-supported nanomechanical resonators. *J. Vac. S. Tech. B* **31**, 051805 (2013).
34. Vansteenkiste, A. *et al.* The design and verification of MuMax3. *AIP Adv.* **4**, 107133 (2014).